Journal of Advanced Ceramics
2020, **9**(4): 424–431
https://doi.org/10.1007/s40145-020-0382-9

ISSN 2226-4108
CN 10-1154/TQ

Research Article

Enhanced thermoelectric properties of hydrothermally synthesized n-type Se&Lu-codoped Bi_2Te_3

Xiaolei SHI[a,†], Xin AI[b,†], Qihao ZHANG[c,d,*], Xiaofang LU[a], Shijia GU[e], Li SU[a], Lianjun WANG[a,f,*], Wan JIANG[a,e]

[a]*State Key Laboratory for Modification of Chemical Fibers and Polymer Materials*, *College of Materials Science and Engineering*, *Donghua University*, *Shanghai 201620*, *China*
[b]*College of Information Science and Technology*, *Donghua University*, *Shanghai 201620*, *China*
[c]*State Key Laboratory of High Performance Ceramics and Superfine Microstructure*, *Shanghai Institute of Ceramics*, *Chinese Academy of Sciences*, *Shanghai 200050*, *China*
[d]*Center of Materials Science and Optoelectronics Engineering*, *University of Chinese Academy of Sciences*, *Beijing 100049*, *China*
[e]*Institute of Functional Materials*, *Donghua University*, *Shanghai 201620*, *China*
[f]*Engineering Research Center of Advanced Glasses Manufacturing Technology*, *Ministry of Education*, *Shanghai 201620*, *China*

Received: January 20, 2020; Revised: April 10, 2020; Accepted: April 22, 2020

Abstract: N-type Se&Lu-codoped Bi_2Te_3 nanopowders were prepared by hydrothermal method and sintered by spark plasma sintering technology to form dense samples. By further doping Se element into Lu-doped Bi_2Te_3 samples, the thickness of the nanosheets has the tendency to become thinner. The electrical conductivity of $Lu_{0.1}Bi_{1.9}Te_{3-x}Se_x$ material is reduced with the increasing Se content due to the reduced carrier concentration, while the Seeback coefficient values are enhanced. The lattice thermal conductivity of the $Lu_{0.1}Bi_{1.9}Te_{3-x}Se_x$ is greatly reduced due to the introduced point defects and atomic mass fluctuation. Finally, the $Lu_{0.1}Bi_{1.9}Te_{2.7}Se_{0.3}$ sample obtained a maximum *ZT* value of 0.85 at 420 K. This study provides a low-cost and simple low-temperature method to mass production of Se&Lu-codoped Bi_2Te_3 with high thermoelectric performance for practical applications.

Keywords: thermoelectric material; n-type; bismuth telluride; hydrothermal synthesis; co-doping

1 Introduction

With the rapid development of society, the gradual consumption of the earth's resources and the energy crisis gradually emerge, so the development of energy materials is very important. The current types of energy materials are various, and energy materials based on thermoelectric materials are gradually entering the field of vision [1]. Thermoelectric materials are special materials that can convert thermal energy and electrical energy into each other. In the category of thermoelectric materials, Bi_2Te_3 and its solid solution alloys have been greatly developed [2]. Bi_2Te_3-based alloys are the

† Xiaolei Shi and Xin Ai contributed equally to this work.

* Corresponding authors.
E-mail: Q. Zhang, zhangqh@mail.sic.ac.cn;
L. Wang, wanglj@dhu.edu.cn

most widely used thermoelectric material at room temperature, and have been often used for power generation in precision instruments. Thermoelectric materials are classified into n-type and p-type according to different conductivity mechanisms. N-type is conductive by electrons, and p-type is conductive by holes. At present, p-type Bi_2Te_3 has been greatly developed [3,4]. The highest record for the *ZT* value is 1.96 at 420 K and an average *ZT* of 1.77 over the temperature range of 320–500 K. However, the performance of n-type Bi_2Te_3 is still at a low level [5,6]. A thermoelectric device is composed of n-type and p-type materials, so it is very necessary to further study the n-type Bi_2Te_3 alloys.

The microstructure of n-type Bi_2Te_3 solid solution typically consists of a multi-layered structure, resulting in an anisotropic thermoelectric material [7]. The composition along the *C*-axis is: –Te(1)–Bi–Te(2)–Bi–Te(1)– [8]. Recent studies show that different layers are connected by van der Waals-like force, and the chemical bonding between the in-plane atoms could be the metavalent bonding [6,9]. Due to the anisotropy caused by its special structure, the physical properties are different in parallel and perpendicular to the interlayer.

It is well known that the properties of thermoelectric materials are usually determined by a dimensionless figure-of-merit coefficient: *ZT*, defined as $ZT = \sigma S^2 T/\kappa$, where T is the absolute temperature, σ is the conductivity, S is the Seebeck coefficient, and κ is the thermal conductivity [1]. Due to the low reserves of Te element, it is essential and necessary to reduce the content of Te in Bi_2Te_3 materials while maintaining the thermoelectric properties. In previous reports, the *ZT* value of the material is increased by doping different elements [10–15]. For example, Se element doping can increase the electron and phonon scattering by forming various point defects in the crystal lattice. N-type $Bi_2Te_{3-x}Se_x$ has been produced and the highest *ZT* value of about 1.2 was achieved by the hot deforming process [16,17]. In some work, the thermoelectric properties of Bi_2Te_3 can be improved by doping rare earth elements, R (R = Lu, Ce, Sm, Er, La, etc.) [18–21]. For example, Ivanov and Yaprintsev [22] prepared $Lu_xBi_{2-x}Te_3$ and a maximum *ZT* value of 0.9 was obtained with the Lu doping amount of 0.1. Ji *et al.* [18] reported an n-type $Lu_xBi_{2-x}Te_3$ TE material with a high *ZT* value of 1.3 at 448 K by hot pressing. However, since the thermal conductivity and electrical conductivity of the Bi_2Te_3-based alloys are anisotropic, the *ZT* value is usually anisotropic. Therefore, when researching the Bi_2Te_3-based solid solution, electrical and thermal properties should be measured in the same direction.

In this work, we prepared the n-type $Lu_{0.1}Bi_{1.9}Te_{3-x}Se_x$ (x = 0, 0.2, 0.3, 0.4) alloys by hydrothermal method combined with spark plasma sintering, and studied the electrical and thermal properties in the same direction (perpendicular to the pressing direction). Se is used as the co-doping element for $Lu_{0.1}Bi_{1.9}Te_3$, which could not only adjust the carrier concentration but also introduce point defects and atomic mass fluctuation to effectively enhance the phonon scattering and reduce the lattice thermal conductivity. The alloy powders were sintered into the bulk with a layered structure. As a result, a maximum *ZT* value of 0.85 is achieved for $Lu_{0.1}Bi_{1.9}Te_{2.7}Se_{0.3}$ at 420 K.

2 Materials and methods

2. 1 Preparation of $Lu_{0.1}Bi_{1.9}Te_{3-x}Se_x$ bulk samples

$BiCl_3$, Na_2TeO_3, $LuCl_3{\cdot}6H_2O$, Na_2SeO_3 were weighed according to the chemical formula. NaOH was used as the pH-controller. PVP was used as the surfactant, and the weighed raw material was dissolved in 400 mL ethylene glycol. After stirring for several hours, the solution was transferred into a 200 mL-polytetrafluoroethylene-lined stainless steel autoclave. The autoclave was sealed and then heated under a temperature of 180 ℃ for 24 h. The nanopowders were separated by a centrifuge, and the black product obtained by centrifugation was repeatedly washed with absolute ethanol and deionized water in order to sufficiently remove residual NaOH and PVP. After the above steps, the obtained powders were placed in a vacuum drying oven at a temperature of 60 ℃ for 6 h. The dried product was then placed in a tube furnace and annealed at 360 ℃ for 6 h under a mixed reducing atmosphere of 5% H_2 and 95% Ar gases. After cooling to room temperature, the obtained powders were sintered using spark plasma sintering (SPS) technology. The highest sintering temperature is 380 ℃ with a pressure of 70 MPa, and the holding time is 5 min. The cylinder-shaped bulk samples of Ø12 mm × 15 mm were finally obtained.

2. 2 Characterization

The phases of as-synthesized powders and bulk samples were characterized by X-ray diffraction (XRD, Rigaku D/Max-2550 PC, Japan) with Cu Kα radiation at 40 kV, 200 mA. The morphology of powders was characterized using field emission scanning electron microscopy (FE-SEM, JSM-6700F, Japan). The TE properties of all bulk samples were measured in the temperature range 300–480 K. The thermal conductivity was calculated by combining thermal diffusivity, specific heat, and sample density according to $\kappa = D \times C_p \times \rho$, where D is the thermal diffusivity coefficient, C_p is the specfic heat capacity, and ρ is the density measured by Archimedes method. A laser flash apparatus (Netzsch LFA 457, Selb, Germany) was employed to obtain the thermal diffusivity. C_p was determined from Ref. [23]. The electrical conductivity and Seebeck coefficient were simultaneously measured by standard four-probe methods under a helium atmosphere using ZEM-3 equipment (ULVAC-RIKO, Japan) after samples were cut into rectangles of about 3 mm × 2 mm × 8 mm. The Hall coefficient R_H was measured on a Lake Shore 8400 system (Lake Shore Design Inc. USA) with a reversible magnetic field of 2 T and an electrical current of 10 mA.

3 Results and discussion

XRD patterns of the $Lu_{0.1}Bi_{1.9}Te_{3-x}Se_x$ powders are shown in Figs. 1(a) and 1(b). As we can see from Fig. 1(a), the main diffraction peaks of the $Lu_{0.1}Bi_{1.9}Te_3$ sample are consistent with the standard JCPDS card (PDF#15-0863) of Bi_2Te_3, indicating the doping of Lu does not change the crystal structure. The main diffraction peaks of the $Lu_{0.1}Bi_{1.9}Te_{3-x}Se_x$ (x = 0.2, 0.3, 0.4) samples are all consistent with the standard JCPDS card (PDF#50-0953) of Bi_2SeTe_2, and no visible impurity phases are observed from XRD. From the enlarged XRD pattern, as shown Fig. 1(b), it can be

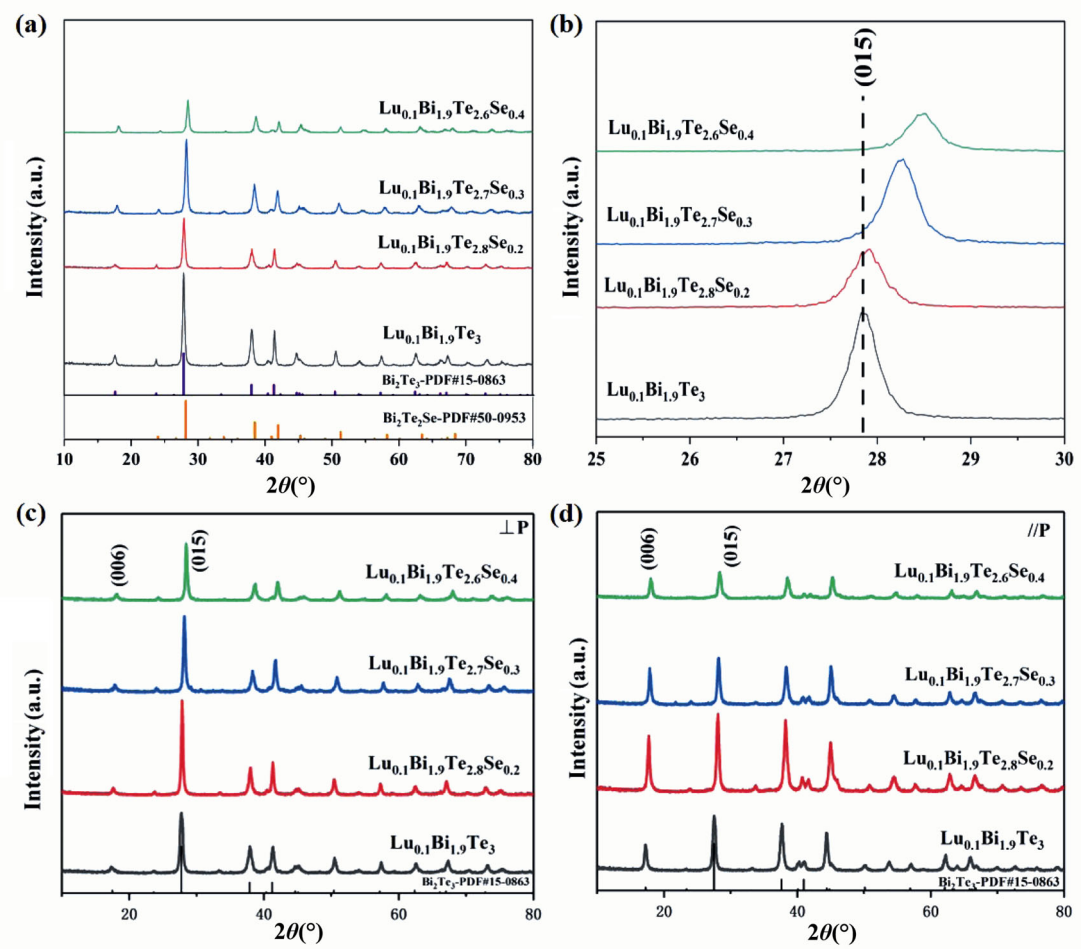

Fig. 1 (a) XRD patterns of $Lu_{0.1}Bi_{1.9}Te_{3-x}Se_x$ (x = 0, 0.2, 0.3, 0.4) powders; (b) the enlarged view of the (015) diffraction peak. XRD patterns of bulk $Lu_{0.1}Bi_{1.9}Te_{3-x}Se_x$ samples taken in the surface that is (c) perpendicular to the pressure direction and (d) parallel to the pressure direction.

seen that the strongest peak in the vicinity of 28° shifts toward high diffraction angles with the increase of Se content. The lattice parameters of all samples were extrapolated from Rietveld refinement and shown in Fig. S1 in the Electronic Supplementary Material. For the Se free sample, the lattice parameters of *a*/*b* and *c* are determined to be 4.369 Å and 30.434 Å, respectively, both of which decrease with rising Se content *x* due to the fact that the radius of Se is smaller than that of Te [11].

Because the Bi_2Te_3-based thermoelectric material usually has the anisotropy feature, XRD analysis was performed on the surfaces of all bulk $Lu_{0.1}Bi_{1.9}Te_{3-x}Se_x$ samples in the direction parallel and perpendicular to SPS-pressuring direction, respectively. As is seen from Figs. 1(c) and 1(d), the grains in different directions undergo different orientation growth during the high-temperature and high-pressure sintering. It can be found that the diffraction intensity shows an obviously difference in the two different directions. Typically, the strongest diffraction peak of (015) observed in the perpendicular direction becomes weaker in the parallel direction, while the diffraction peak of (006) gets stronger, proving the anisotropy feature of the $Lu_{0.1}Bi_{1.9}Te_{3-x}Se_x$ bulk samples.

SEM images of all $Lu_{0.1}Bi_{1.9}Te_{3-x}Se_x$ nanopowders are shown in Fig. 2. We can see that the morphology of all powders shows the appearance of nanosheets. This is consistent with the relevant reports that the composition along the *C*-axis is: –Te(1)–Bi–Te(2)–Bi–Te(1)– and different layers are connected by the van der Waals-like force, while the atoms within the layer are connected by metavalent bonding [6]. Because the energy for breaking the van der Waals bond is much lower than the energy required for breaking the covalent bond, Bi_2Te_3 grains tend to grow along the *a*- and *b*-axis. It also can be seen that, with the increasing content of Se element, the morphology of the nanosheets has changed from wafer shape to hexagonal sheet. This may be caused by the fact that Se and Te are the same group element, and the elemental properties are not much different, which contributes to the formation of the regular hexagon [24]. However, due to the agglomeration of the nanosheets, it is difficult to identify their size and distribution. But it is clearly seen from the SEM images that the thickness of nanosheets has the tendency to become thinner.

The EDS element mapping results of bulk $Lu_{0.1}Bi_{1.9}Te_{2.7}Se_{0.3}$ sample are presented in Fig. 3, which can prove whether the Lu element and Se element enter the lattice and show the distribution of each element. We can see that each element is evenly distributed without obvious agglomeration. Besides, it can be seen from Fig. 3(f) that the nanoparticles are oriented and rearranged after the sintering process. Due to special layered structure, the thermoelectric properties in different directions should be different.

Figure 4(a) presents the temperature dependence of electrical conductivity for all bulk samples. The electrical conductivity values of the samples decrease with increasing measuring temperature, indicating a metallic transport behavior. The decrease of σ with

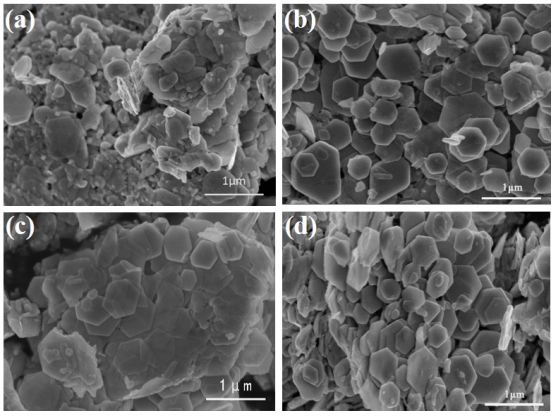

Fig. 2 SEM images of the nanopowders: (a) $Lu_{0.1}Bi_{1.9}Te_3$; (b) $Lu_{0.1}Bi_{1.9}Te_{2.8}Se_{0.2}$; (c) $Lu_{0.1}Bi_{1.9}Te_{2.7}Se_{0.3}$; (d) $Lu_{0.1}Bi_{1.9}Te_{2.6}Se_{0.4}$.

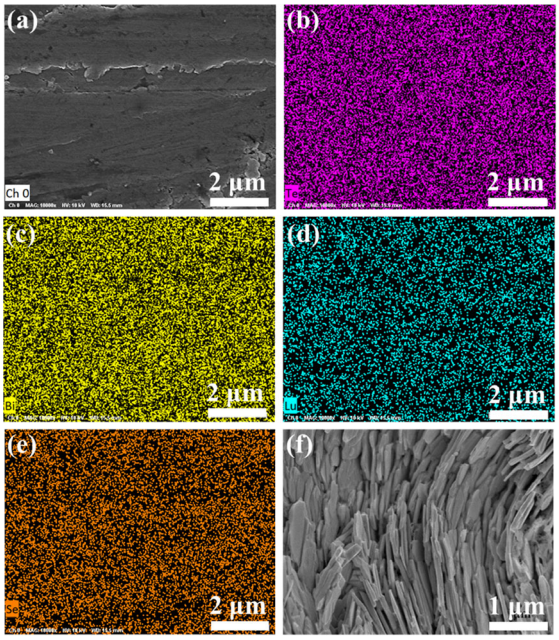

Fig. 3 EDS element mapping of the bulk $Lu_{0.1}Bi_{1.9}Te_{2.7}Se_{0.3}$ sample: (a) scanning area; (b) Te; (c) Bi; (d) Lu; (e) Se. (f) SEM image of the fractured surface of bulk $Lu_{0.1}Bi_{1.9}Te_{2.7}Se_{0.3}$.

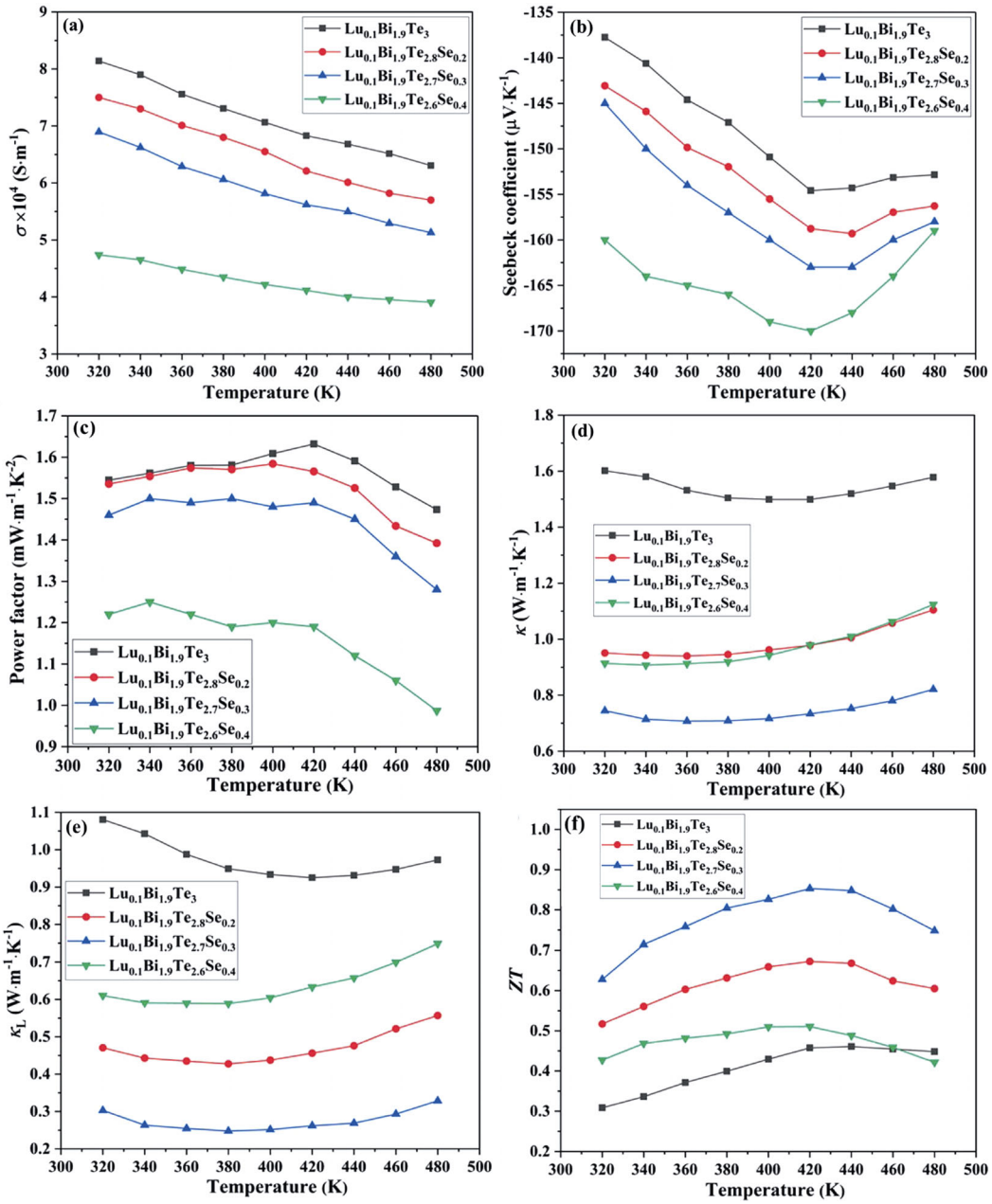

Fig. 4 Temperature-dependent thermoelectric properties of all bulk samples: (a) electrical conductivity; (b) Seebeck coefficient; (c) power factor; (d) total thermal conductivity; (e) lattice thermal conductivity; (f) *ZT*.

increasing temperature can be related to the carrier scattering by phonons [1,25]. As we all know that the electrical conductivity can be expressed as $\sigma = ne\mu$, where n, e, and μ are carrier concentration, the electron charge, and carrier mobility, respectively [26]. Using the Hall effect to determine the samples' electron carrier concentration and mobility, the results are 9.34, 7.18, 6.75, 6.5 ($\times10^{19}$cm^{-3}) and 58.3, 56.4, 55.79, 54.49 (cm^2/(V·s)) for $Lu_{0.1}Bi_{1.9}Te_3$, $Lu_{0.1}Bi_{1.9}Te_{2.8}Se_{0.2}$, $Lu_{0.1}Bi_{1.9}Te_{2.7}Se_{0.3}$, $Lu_{0.1}Bi_{1.9}Te_{2.6}Se_{0.4}$, respectively. The decreased carrier concentration with increasing Se content in this work might be attributed to the inhibited donor-like effect [11]. With more Te replaced by Se, the differences of both the electronegativity and atom size between the anion and cation increase. Thus, the formation of antisite defects is suppressed, associated with the promotion of anion vacancies, which weakens the contribution of the donor-like effects and decreases the electron density. Consequently, a lower carrier concentration is obtained in samples with higher Se contents. Meanwhile, there is no significant change in carrier mobility. Through the combined effects of

carrier concentration and mobility, the electrical conductivity of $Lu_{0.1}Bi_{1.9}Te_{3-x}Se_x$ (x = 0.2, 0.3, 0.4) is reduced compared to that of the $Lu_{0.1}Bi_{1.9}Te_3$ sample.

Figure 4(b) presents the temperature dependences of Seebeck coefficient for all bulk samples. The result indicates that the Seebeck coefficient values for all samples present negative value which confirms that electrons are the major transportation carriers. It is known that the Seebeck coefficient can be expressed by Eq. (1)

$$\alpha = \frac{8\pi^2 k_B^2}{3eh^2} m^* T \left(\frac{\pi}{3n}\right)^{\frac{2}{3}} \left(\frac{3}{2} + \gamma\right) \quad (1)$$

where k_B is the Boltzmann constant, h is the Planck's constant, and γ is the scattering parameter [27]. The absolute Seeback coefficient values of all samples increase first then decrease with the increasing temperature. This is because between 300 and 420 K, impurity ionization becomes more pronounced with increasing temperature, and scattering of carriers is enhanced, so the Seebeck coefficient is increased [3]. As the temperature increases, the valence band and the conduction band will produce a thermal excitation effect of the charge carrier, thereby generating electrons in the conduction band and holes in the valence band, which increases the carrier concentration and leads to the decrease of Seebeck coefficient. After the doping of Se, the carrier concentration of the sample is reduced, resulting in the increase of Seebeck coefficient. The calculated power factor ($PF = \alpha^2\sigma$) values for all bulk samples are shown in Fig. 4(c). It can be seen that the power factor of $Lu_{0.1}Bi_{1.9}Te_{3-x}Se_x$ (x = 0.2, 0.3, 0.4) is reduced compared to that of the $Lu_{0.1}Bi_{1.9}Te_3$ sample. This is because the increase in the Seebeck coefficient of the Se-doped $Lu_{0.1}Bi_{1.9}Te_3$ sample is less than the decrease in the electrical conductivity.

Because the thermoelectric properties of n-type Bi_2Te_3-based alloys are anisotropic, the κ together with α and σ is measured in the same testing direction (perpendicular to pressing direction). The temperature-dependent behavior of the thermal conductivity (shown in Fig. 4(d)) revealed that all bulk samples are crystalline materials, because the curves first decrease with increasing temperature and then increase. The electronic thermal conductivity (κ_e) is related to the specific electrical conductivity, according to the Wiedemann–Franz law $\kappa_e = L\sigma T$ [28], where L is the Lorenz number. The Lorenz number used in this work is 2.45×10^{-8} W·Ω·K^{-2}. Then, the lattice contribution (κ_L) to the total thermal conductivity can be calculated by $\kappa_L = \kappa - \kappa_e$. As presented in Fig. 4(e), the lattice thermal conductivity of the $Lu_{0.1}Bi_{1.9}Te_{3-x}Se_x$ (x = 0.2, 0.3, 0.4) samples decreases compared with that of the $Lu_{0.1}Bi_{1.9}Te_3$ sample, which results in the decreased total thermal conductivity (Fig. 4(d)). The decreased lattice thermal conductivity could be caused by the point defects that are produced due to the additional Se doping, and the mass fluctuation between different atoms, which jointly contribute to more intense phonon scattering [2,3]. Specially, the lattice thermal conductivity of $Lu_{0.1}Bi_{1.9}Te_{2.7}Se_{0.3}$ is about 51.6% lower than that of the $Lu_{0.1}Bi_{1.9}Te_3$ sample.

The calculated ZT values of all samples are shown in Fig. 4(f). The temperature-dependent behavior of ZT for all samples show that ZT first increases with increasing temperature, and then decreases. The maximum ZT value for $Lu_{0.1}Bi_{1.9}Te_{2.7}Se_{0.3}$ is 0.85 at 420 K, increased by about 47.5% compared to that of $Lu_{0.1}Bi_{1.9}Te_3$ samples, which is also higher than the reported value of 0.68 for $Lu_{0.1}Bi_{1.9}Te_{2.7}Se_{0.3}$ sample in Ref. [25].

Furthermore, we repeated three times tests of thermoelectric properties of the $Lu_{0.1}Bi_{1.9}Te_{2.7}Se_{0.3}$ sample. The electrical conductivity, Seebeck coefficient, power factor, lattice thermal conductivity, total thermal conductivity, and ZT are shown in Fig. 5. The results show that the $Lu_{0.1}Bi_{1.9}Te_{2.7}Se_{0.3}$ sample prepared in this work has good repeatability.

4 Conclusions

In this study, we have succeeded in fabricating the n-type $Lu_{0.1}Bi_{1.9}Te_{3-x}Se_x$ (x = 0, 0.2, 0.3, 0.4) nanopowders using eco-friendly and cost-effective hydrothermal approach and densifying the nanopowders by spark plasma sintering. By further doping the Se element, the Seebeck coefficient of $Lu_{0.1}Bi_{1.9}Te_3$ matrix is enhanced due to the decreased carrier concentration while the lattice thermal conductivity is greatly reduced by more intense phonon scattering. A maximum ZT value of 0.85 is obtained for Se&Lu-codoped Bi_2Te_3 at 420 K, increased by about 47.5% compared to that of pristine single-element Lu-doped Bi_2Te_3 sample, which shows great potential for low-temperature thermoelectric applications.

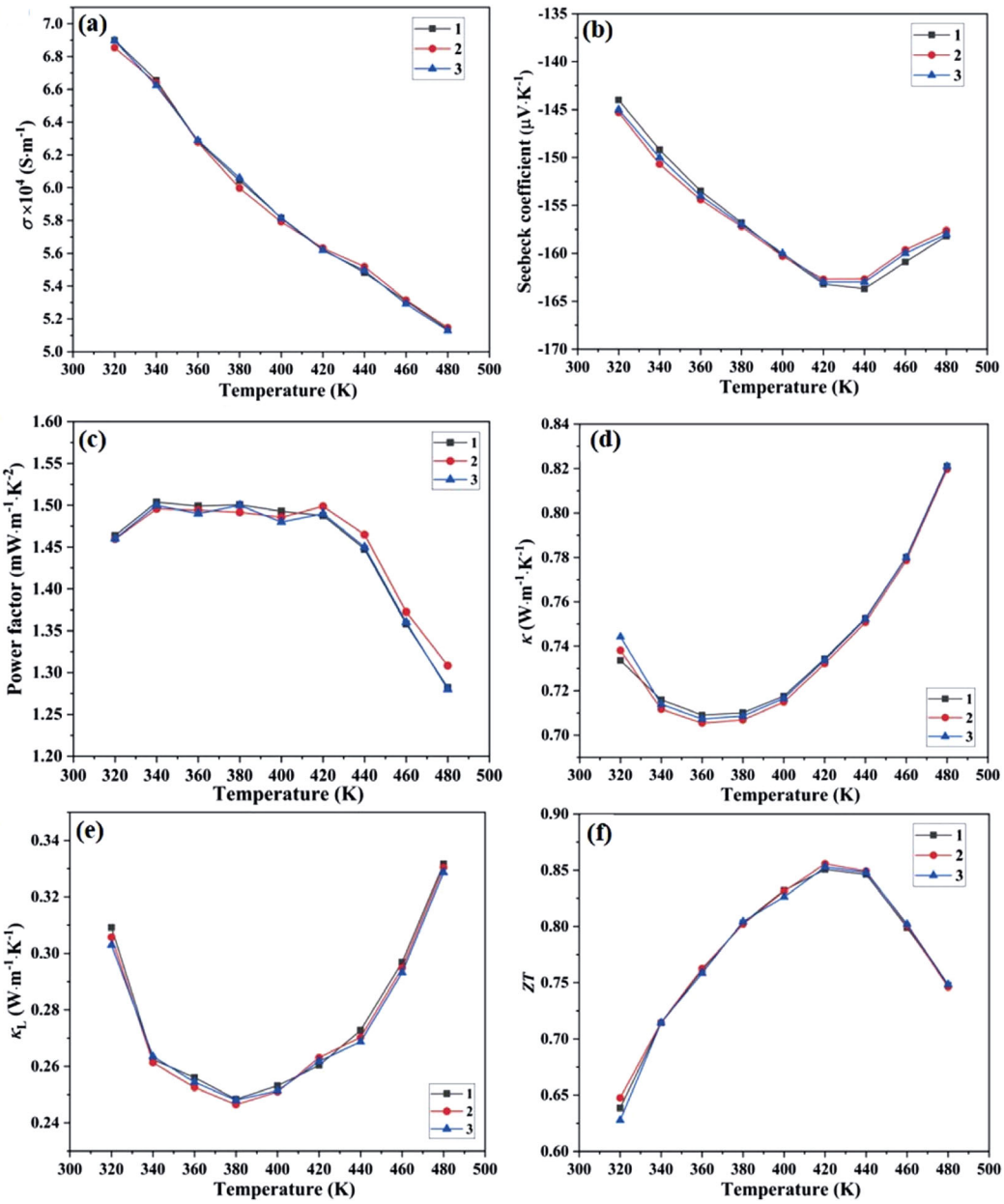

Fig. 5 Repeated tests of thermoelectric properties of $Lu_{0.1}Bi_{1.9}Te_{2.7}Se_{0.3}$ sample: (a) electrical conductivity; (b) Seebeck coefficient; (c) power factor; (d) thermal conductivity; (e) lattice thermal conductivity; (f) *ZT*.

Acknowledgements

This work was funded by the Fundamental Research Funds for the Central Universities (No. 2232020A-02), National Natural Science Foundation of China (Nos. 51774096, 51871053, 51902333), Shanghai Committee of Science and Technology (18JC1411200), Program for Innovative Research Team in University of Ministry of Education of China (IRT_16R13). Q. Zhang acknowledges financial support sponsored by Shanghai Saiiling Program (19YF1454000) and Key Research Program of Frontier Sciences, CAS (Grant No. ZDBS-LY-JSC037).

Electronic Supplementary Material

Supplementary material is available in the online version of this article at https://doi.org/10.1007/s40145-020-0382-9.

References

[1] Snyder GJ, Toberer ES. Complex thermoelectric materials. *Nat Mater* 2008, **7**: 105–114.

[2] Zhu TJ, Liu YT, Fu CG, *et al*. Compromise and synergy in high-efficiency thermoelectric materials. *Adv Mater* 2017, **29**: 1605884.

[3] Fang T, Li X, Hu CL, *et al*. Complex band structures and lattice dynamics of Bi_2Te_3-based compounds and solid solutions. *Adv Funct Mater* 2019, **29**: 1900677.
[4] Deng RG, Su XL, Hao SQ, *et al*. High thermoelectric performance in $Bi_{0.46}Sb_{1.54}Te_3$ nanostructured with ZnTe. *Energy Environ Sci* 2018, **11**: 1520–1535.
[5] Min Y, Roh JW, Yang H, *et al*. Surfactant-free scalable synthesis of Bi_2Te_3 and Bi_2Se_3 nanoflakes and enhanced thermoelectric properties of their nanocomposites. *Adv Mater* 2013, **25**: 1425–1429.
[6] Yu Y, Cagnoni M, Cojocaru-Mirédin O, *et al*. Chalcogenide thermoelectrics empowered by an unconventional bonding mechanism. *Adv Funct Mater* 2020, **30**: 1904862.
[7] Scherrer H. *CRC Handbook of Thermoelectrics*. CRC Press, 1995.
[8] Nolas GS, Sharp J, Goldsmid HJ. *Thermoelectrics*. Springer Berlin Heidelberg, 2001.
[9] Cheng YD, Cojocaru-Mirédin O, Keutgen J, *et al*. Understanding the structure and properties of sesqui-chalcogenides (i.e., V_2VI_3 or Pn_2Ch_3 (Pn = pnictogen, Ch = chalcogen) compounds) from a bonding perspective. *Adv Mater* 2019, **31**: 1904316.
[10] Zhang Z, Duan XM, Qiu BF, *et al*. Preparation and anisotropic properties of textured structural ceramics: A review. *J Adv Ceram* 2019, **8**: 289–332.
[11] Pan Y, Wei TR, Wu CF, *et al*. Electrical and thermal transport properties of spark plasma sintered n-type $Bi_2Te_{3-x}Se_x$ alloys: The combined effect of point defect and Se content. *J Mater Chem C* 2015, **3**: 10583–10589.
[12] Xiao YK, Chen GX, Qin HM, *et al*. Enhanced thermoelectric figure of merit in p-type $Bi_{0.48}Sb_{1.52}Te_3$ alloy with WSe_2 addition. *J Mater Chem A* 2014, **2**: 8512–8516.
[13] Zhuang HL, Pan Y, Sun FH, *et al*. Thermoelectric Cu-doped $(Bi,Sb)_2Te_3$: Performance enhancement and stability against high electric current pulse. *Nano Energy* 2019, **60**: 857–865.
[14] Zhang CH, Zhang CX, Ng H, *et al*. Solution-processed n-type $Bi_2Te_{3-x}Se_x$ nanocomposites with enhanced thermoelectric performance via liquid-phase sintering. *Sci China Mater* 2019, **62**: 389–398.
[15] Yoon JS, Song JM, Rahman JU, *et al*. High thermoelectric performance of melt-spun $Cu_xBi_{0.5}Sb_{1.5}Te_3$ by synergetic effect of carrier tuning and phonon engineering. *Acta Mater* 2018, **158**: 289–296.
[16] Hu LP, Zhu TJ, Liu XH, *et al*. Point defect engineering of high-performance bismuth-telluride-based thermoelectric materials. *Adv Funct Mater* 2014, **24**: 5211–5218.
[17] Tang ZL, Hu LP, Zhu TJ, *et al*. High performance n-type bismuth telluride based alloys for mid-temperature power generation. *J Mater Chem C* 2015, **3**: 10597–10603.
[18] Ji XH, Zhao XB, Zhang YH, *et al*. Synthesis and properties of rare earth containing Bi_2Te_3 based thermoelectric alloys. *J Alloys Compd* 2005, **387**: 282–286.
[19] Ji XH, Zhao XB, Zhang YH, *et al*. Solvothermal synthesis and thermoelectric properties of lanthanum contained Bi–Te and Bi–Se–Te alloys. *Mater Lett* 2005, **59**: 682–685.
[20] Wu F, Song HZ, Jia JF, *et al*. Effects of Ce, Y, and Sm doping on the thermoelectric properties of Bi_2Te_3 alloy. *Prog Nat Sci: Mater Int* 2013, **23**: 408–412.
[21] Yang JJ, Wu F, Zhu Z, *et al*. Thermoelectrical properties of lutetium-doped Bi_2Te_3 bulk samples prepared from flower-like nanopowders. *J Alloys Compd* 2015, **619**: 401–405.
[22] Ivanov O, Yaprintsev M. Mechanisms of thermoelectric efficiency enhancement in Lu-doped Bi_2Te_3. *Mater Res Exp* 2018, **5**: 015905.
[23] Hong M, Chen ZG, Yang L, *et al*. $Bi_xSb_{2-x}Te_3$ nanoplates with enhanced thermoelectric performance due to sufficiently decoupled electronic transport properties and strong wide-frequency phonon scatterings. *Nano Energy* 2016, **20**: 144–155.
[24] Cao RJ, Song HZ, Gao WX, *et al*. Thermoelectric properties of Lu-doped n-type $Lu_xBi_{2-x}Te_{2.7}Se_{0.3}$ alloys. *J Alloys Compd* 2017, **727**: 326–331.
[25] Vasil'Ev A, Yaprintsev M, Ivanov O, *et al*. Anisotropic thermoelectric properties of $Bi_{1.9}Lu_{0.1}Te_{2.7}Se_{0.3}$ textured via spark plasma sintering. *Solid State Sci* 2018, **84**: 28–43.
[26] Tang CM, Liang DD, Li HZ, *et al*. Preparation and thermoelectric properties of $Cu_{1.8}S/CuSbS_2$ composites. *J Adv Ceram* 2019, **8**: 209–217.
[27] Park KC, Dharmaiah P, Kim HS, *et al*. Investigation of microstructure and thermoelectric properties at different positions of large diameter pellets of $Bi_{0.5}Sb_{1.5}Te_3$ compound. *J Alloys Compd* 2017, **692**: 573–582.
[28] Liu WS, Yan X, Chen G, *et al*. Recent advances in thermoelectric nanocomposites. *Nano Energy* 2012, **1**: 42–56.